

# Vortex-induced vibrations of a deformable splitter plate behind a square cylinder controlled by active pitch oscillation

Aravindhana Venkatesh<sup>1</sup>, Hua-Dong Yao<sup>1\*</sup>, Jiqiang Niu<sup>2,3</sup>,  
Xiao Xue<sup>1</sup>

<sup>1</sup>\*Department of Mechanics and Maritime Sciences, Chalmers University of Technology, Gothenburg, 42196, Sweden.

<sup>2</sup>School of Mechanical Engineering, Southwest Jiaotong University, Chengdu, 610031, Sichuan Province, China.

<sup>3</sup>Maglev Technology Key Laboratory of Railway Industry, Tongji University, Shanghai, 201804, China.

\*Corresponding author(s). E-mail(s): [huadong.yao@chalmers.se](mailto:huadong.yao@chalmers.se);

## Abstract

Vortex-induced vibrations (VIV) widely occur in nature and are of interest for energy harvesting and bio-inspired propulsion. To understand passive VIV coexisting with active structure motions, this paper is motivated to numerically investigate the use of pure pitch oscillation to control a square cylinder mounted with a deformable splitter plate at the Reynolds number of 333. Direct numerical simulations using a partitioned method with a semi-implicit coupling algorithm are performed. According to the trajectories of the splitter-plate tip displacement with respect to the lift or drag force coefficient, a specific lock-in regime determined by the frequency of the enforced pitch oscillation is identified. Further spectral analyses of the tip displacement and lift force show that the lock-in frequencies are equal to the enforced frequencies. Next to the lock-in regime, semi-lock-in regimes with narrow bandwidths are distinguished, exhibiting both lock-in and non-lock-in features. In the non-lock-in regimes, the frequencies of the most predominant peaks in the spectra are found near the natural frequency of the splitter plate, and the frequencies of the two secondary peaks are distributed along the characteristic lines following the ratios of these frequencies to the enforced frequency, which are  $\pm 1$ . Thus, the interaction is dependent on the combined effects of the passive VIV and the actively enforced pitch oscillations. Moreover, the intersection points of the characteristic lines are located

close to the upper and lower frequency limits of the lock-in regime, inferring the conditions for the lock-in onset.

**Keywords:** Actively enforced pitch, deformable splitter plate, lock-in, secondary frequencies, square cylinder, vortex-induced vibration

## 1 Introduction

Vortex-induced vibration (VIV) is a typical phenomenon of fluid-structure interaction (FSI) in flow past a blunt body where vortices induced by the body result in self-sustained vibration of the body. It exists in vast applications such as offshore structures, renewable energy harvesting, biomedical devices, aircraft, etc. VIV is categorized into flutter, galloping and buffeting in terms of vibration frequency and amplitudes [1, 2]. A benchmark case of VIV is a deformable splitter plate assembled onto the rear side of a square cylinder. Since this configuration setup induces flow possessing plenty of representative mechanisms, it has been widely investigated and considered in the validation of numerical and experimental FSI methods [see 3–10].

Matthies and Steindorf [4] proposed an implicit coupling (also termed strongly coupling) algorithm on the basis of a nonlinear block Newton algorithm, to develop a partitioned strategy for FSI simulation. One of the validation cases in their study is the benchmark VIV case of the square cylinder with the splitter plate at the Reynolds number,  $Re$ , of 333. In the partitioned strategy, the flow and structure deformations are separately solved with different solvers but coupled by iterating variables at the interfaces between the fluid and structure. Dettmer and Perić [5] took advantage of this benchmark VIV case to validate a partitioned approach with an implicit coupling algorithm. Both flow and solid solvers were implemented based on finite-element discretization. Stabilised low order velocity–pressure finite elements were considered to discretize the incompressible Navier–Stokes equations, and standard finite element approximations for the structure. An arbitrary Lagrangian–Eulerian (ALE) strategy was used to capture the flow domain deformation. A discrete implicit generalised- $\alpha$  method was taken for the temporal discretization of both solvers. In the study by Wood et al. [7], this benchmark VIV case was simulated using a partitioned approach. An implicit coupling algorithm called the block-Gauss-Seidel (BGS) algorithm was adopted to couple fluid and solid solvers. An incompressible finite volume method (FVM) with an ALE algorithm on deformable fluid-solid interfaces was utilized for the flow solver, and a finite element method (FEM) for large dynamic structural deformation was for the solid solver. Later, considering the same VIV case, Kassiotis et al. [8] compared the BGS and explicit algorithms. Habchi et al. [9] studied a similar partitioned approach implemented in the open-source tool OpenFOAM, and validated the approach based on this benchmark case. The incompressible flow was solved with the PIMPLE algorithm, and the large structural deformation using the Saint Venant–Kirchhoff constitutive model. A dynamic Aitken method was applied to accelerate the coupling iteration between the solvers. Their method has also been testified for a biomechanics application with large deformations [11]. A monolithic approach for FSI

simulation was proposed by Schott et al. [10]. One of the cases for the method validation is this benchmark case. In their study, the monolithic approach was implemented for FEM, but it is generally applicable for other discretization schemes.

The square cylinder with the flexible splitter plate has been considered to develop a concept for piezoelectric energy harvesters [12], where the strain energy from plate deformations is harvested by piezoelectric patches on the polymeric splitter plate. Previous harvesters of this type were installed with rigid splitter plates, which vibrate at relatively higher frequencies. In contrast, the flexible plate of the concept has deformations at low frequencies. Through water-tunnels tests (for  $Re$  between 9200 and 14300) and numerical simulations with a partitioned method coupling the ANSYS modules of Fluent and Mechanical (for  $Re$  between 4974 and 9648), Binyet et al. [12] showed that the power conversion is dependent on the inflow speed and the geometric parameters such as the square width, and the plate length and thickness. The Reynolds-averaged Navier-Stokes (RANS) equations with the realizable  $k$ - $\epsilon$  model were used for the flow simulations. In another work of water-tunnel tests by Binyet et al. [13], this configuration at  $Re$  from 1500 to 19700 was studied to understand how the geometric parameters of the splitter plate affects the flow characteristics and, consequently, the harvested mechanical energy.

Instead of a single set of a flexible plate attached on a square cylinder (i.e., the benchmark case reviewed above), Furquan and Mittal [14] analyzed two sets positioned side by side at  $Re = 100$  using a partitioned FEM approach. Compared to the single set, this two-set case exhibits out-phase vibrations at the initial stage before in-phase vibrations are developed. The lock-in was found by adjusting the plate structure stiffness but retaining the density ratio of the solid to the fluid and the Poisson ratio. Besides, increasing the distance between the two sets results in a reduced vibration amplitude. Sarioglu [15] carried out an experimental study for a square cylinder at various incidence angles from  $0^\circ$  to  $45^\circ$  at  $Re = 3 \times 10^4$ , where a rigid and stationary splitter plate with the same length as the square width is positioned behind the cylinder to passively control vortex formation in the wake. It was found that the splitter plate is effective in reducing the drag at all incidence angles. A reduction of 20% is achieved at the zero incidence angle, and the minimum and maximum reductions are near  $13^\circ$  and  $20^\circ$ , respectively.

Aside from the deformable splitter plate, the details of the rigid splitter plate controlling the vortex shedding from the square cylinder within a plane duct at low  $Re$  between 110 and 200 were explored numerically by Turki [16]. It was found that the length and location of the splitter plate is critical to affecting the vortex shedding and characteristic Strouhal number, as well as drag and lift coefficients. After that, Ali et al. [17] systematically analyzed the effects of the length of the rigid splitter plate varying between 0.5 and 6 times of the square cylinder width at  $Re = 150$  by means of direct numerical simulation (DNS).

In addition to square cylinders, a circular cylinder attached with a deformable splitter plate within a plane channel was put forward as a benchmark VIV case, termed the Turek-Hron benchmark [18]. It has also been widely adopted to validate FSI methods, for example, by Giannelis and Vio [19]. The Turek-Hron benchmark was further modified to generate other VIV cases like the research by Sahu et al. [20], where

the circular cylinder is mounted onto a spring so that a spring-mass system at  $Re = 150$  is established in addition to the flexible splitter plate. By setting slip wall conditions on the side boundaries and increasing the fluid domain size for the Turek-Hron case, Pfister and Marquet [21] analyzed the FSI stability and dynamics for  $Re = 80$ . Recently, Duan and Wang [22] conducted experiments for rigid and flexible plates of different lengths attached onto a circular cylinder, to reduce the noise generated from the flow induced by the cylinder at  $Re$  from  $3.83 \times 10^4$  to  $9.57 \times 10^4$ .

The present study is motivated to understand the interaction between the flow and structural deformation when passive VIV is triggered in combination with active pitch oscillation enforced on the structure. Compared to other research works on similar subjects, we start from the square cylinder body attached with the flexible splitter plate for which an overview of the previous studies is presented above, while these studies focused on a stationary scenario that does not involve enforced oscillations. The previous data of the stationary scenario will support the method validation in this study and be used as a reference to address how the enforced oscillation affects VIV. The aims are to explore the effects of the active pitch oscillation on the passive vibrations of the downstream splitter plate. The changes of the lift and drag forces, as well as the structure deformations, due to the active oscillation will be addressed. Moreover, the onset conditions of the lock-in phenomenon will be understood based on the analysis of variable changes in time and frequency domains. The effects of the enforced pitch frequency on the FSI will be explored in terms of the predominant flow and structure characteristics.

## 2 Application description

The configuration investigated in this study is shown in Fig. 1. A square blunt body is assembled with a splitter plate at the center of the back side of the blunt body. The structure of the blunt body is rigid, whereas the splitter plate is flexible. This combined structure system is forced to oscillate periodically at the center of the joint between the blunt body and splitter plate. The time-varying angle of the rotating pitch oscillation that is actively enforced is defined as:

$$\theta = A \sin(2\pi f_{exc} t), \quad (1)$$

where  $A = 3^\circ$ , and  $f_{exc}$  is prescribed between 0 and 6 Hz.

The width of the square body is  $D$ , and the plate has a length of  $4D$  and a thickness of  $0.06D$ . The Reynolds number is approximately 333, which is calculated based on  $D$  and the freestream flow velocity  $U_0$ . Considering the low Re number, it is reasonable to simulate incompressible and laminar flow past the structure in two dimensions. The characteristic frequency of the flow passing over the square body is  $f_T = U_0/D = 51.3$  Hz.

The splitter plate is regarded to be linear elastic. As the square cylinder is rigid, it has no deformations and is thus excluded from the structural analysis. The mass ratio of the plate structure density to the fluid density is 84.756. The reduced velocity ratio is defined as  $U_0/(f_{n,1}D) = 1.542$ , where  $f_{n,1}$  is the first natural frequency of the

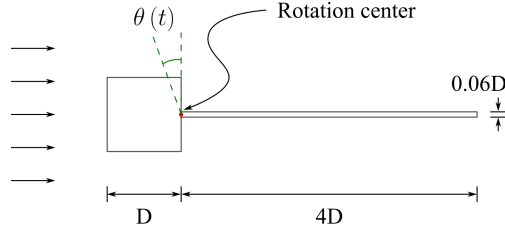


**Fig. 1** Schematic of the square blunt body attached with the flexible plate, where the cylinder is in forced vibration. The arrows upstream of the body indicate the inflow direction. The angle  $\theta(t)$  varies periodically in time.

splitter plate. Young's modulus of the plate is  $2.5 \times 10^5$  Pa, and the Poisson ratio is 0.35.

The setup of the configuration and inflow conditions are established in reference to a benchmark VIV case that was widely investigated, for example, by Wall [3], Matthies and Steindorf [4], Olivier et al. [6], Wood et al. [7], Habchi et al. [9]. The available data will be used for the methodology validation in the following section. However, the forced oscillation has not been introduced in these previous studies.

### 3 Numerical method

#### 3.1 Governing equations

The flow is considered incompressible, two-dimensional and laminar due to the low Reynolds number of  $Re = 333$  in this work. The governing equations of the continuity and momentum in the flow are written as:

$$\frac{\partial u_i}{\partial x_i} = 0, \quad (2)$$

$$\frac{\partial u_i}{\partial t} + u_j \frac{\partial u_i}{\partial x_j} = -\frac{1}{\rho_f} \frac{\partial P}{\partial x_i} + \nu \frac{\partial^2 u_i}{\partial x_j \partial x_j}, \quad (3)$$

where  $u_i$  denotes the  $i$ -indexed component of the velocity vector, and  $P$  is the pressure. The density  $\rho_f$  is constant for the incompressible flow. The kinematic viscosity is denoted by  $\nu$ .

The structure material is linear elastic isotropic. In the structural model, the effects of gravity and structural damping are neglected. The momentum balance equations in the Lagrangian form read:

$$\frac{\partial^2 y_i}{\partial t^2} = \frac{1}{\rho_s} \frac{\partial \sigma_{ij}^s}{\partial x_j}, \quad (4)$$

where  $y_i$  is the  $i$ -indexed component of the displacement vector,  $\rho_s$  is the structure density, and  $\sigma_{ij}^s$  denotes the second-order Cauchy stress tensor. The Saint Venant-Kirchhoff model is used to take into account the geometric nonlinearity that is caused by large structure deflection [23]. The constitutive stress-strain relationship of the

linear elastic model deals with the Green-Lagrange strain tensor  $G_{ij}$ :

$$G_{ij} = \frac{1}{2} \left( \frac{\partial y_i}{\partial x_j} + \frac{\partial y_j}{\partial x_i} + \frac{\partial y_k}{\partial x_i} \frac{\partial y_k}{\partial x_j} \right). \quad (5)$$

The second Piola-Kirchhoff stress tensor is written as

$$S_{ij} = \frac{1}{2} E \left( \frac{1}{(1 + \nu_s)} G_{ij} - \frac{\nu_s}{(1 + \nu_s)(1 - 2\nu_s)} G_{kk} \delta_{ij} \right), \quad (6)$$

where  $E$  is Young's modulus, and  $\nu_s$  is Poisson's ratio.

### 3.2 Partitioned approach of coupled FSI

The simulation of FSI adopts a partitioned approach [24]. In this approach, the fluid and structure are solved separately using different solvers. An ALE algorithm is utilized to describe the continuum mechanics in the progression of the deforming fluid and structure domains in time and space [25, 26]. A semi-implicit method is applied to coupling the fluid and structure solvers [27, 28]. The flow pressure and shear stress tensors are exchanged with the structure displacements on the interfaces between the flow and structure domains, where a space conservative interpolation approach is used to map these variables onto unconfomable mesh cells between the domains [29].

In the flow solver, a finite volume method based on the pressure-based segregated algorithm of semi-implicit method for pressure linked equations (SIMPLE) is used to compute the incompressible laminar flow [30]. A least squares cell-based approach is adopted in the computation of gradients. A second-order upwind scheme is used in the spatial discretization of the momentum equations. The time marching approach is implemented with an implicit scheme.

The structure solver utilizes the finite element method (FEM) [31]. The approximation of the discretized governing equations in a weak form is derived on the basis of the Galerkin method of weighted residuals [32]. The element approximation chooses the same formulations for the weighting and element shape functions. The Gaussian integration method is used to calculate integrals [33]. Dynamic simulation is performed since the splitter-plate structure is subjected to transient dynamic loads from the flow.

### 3.3 Numerical setup

The two-dimensional computational domains of the fluid and structure are sketched in Fig. 2. The domain dimensions and layout are defined in reference to the studies by Ramm and Wall [34] and Bazilevs et al. [35]. The inlet is positioned for 4.5 from the square cylinder, the side boundaries for 5.5, and the outlet for 14. To monitor the flow field, three probes such as P1, P2 and P3 are positioned at  $(x, y) = (0.5, 0.5)$ ,  $(8, 0)$  and  $(0.5, 0.8)$ .

In the flow simulation, the boundary condition (BC) of velocity inlet is set at the inlet of the flow domain, The symmetry BC is set at the side boundaries, and the pressure outlet at the outlet. The under-relaxation factors for the pressure and momentum in the segregated flow solver are set to 0.3 and 0.7. In the structure domain,

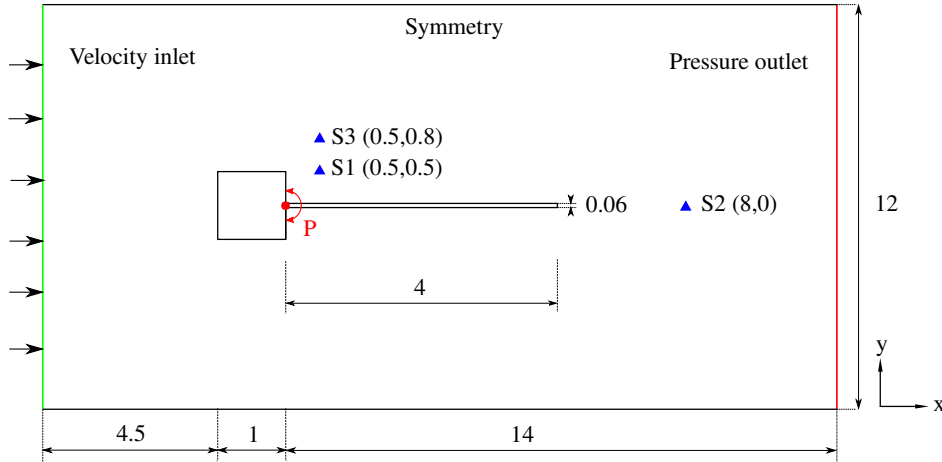


**Fig. 2** Schematic of the fluid and structure computational domains. The dimensions are normalized based on the square cylinder width  $D$ . The triangles mark out the probe positions such as S1, S2 and S3 for monitoring flow variables.

**Table 1** The normalized key cell sizes of the baseline case (i.e., Mesh 3 in Table 2).

Location	Size
Square body surface	0.026 – 0.05
Splitter plate surface <sup>¶</sup>	0.03 – 0.08 (side) 0.003 (tip)
First-layer cell height near walls	0.002
Far-field boundary	0.34
Growth ratio of cell sizes	1.1

<sup>¶</sup> As the splitter plate surface is actually the FSI interface, the cell sizes are used for both fluid and structure meshes.

the time-varying rotation angle, which is predefined in Eq. 1, is set at the interface between the square cylinder back-side and the splitter plate front-side. The rotation center is located at this interface center.

## 4 Method validation

### 4.1 Mesh independence study

Structured meshes are generated in the fluid and structure domains. The Laplacian method is used to update the meshes during the simulation. The dimensionless key cell sizes of the baseline case normalized by the square body length  $D$  are listed in Table 1. The surface cell sizes for the splitter plate are taken to generate both fluid and structure meshes, and the remaining parameters for the generation of the fluid mesh. The growth ratio of the cell sizes in the fluid mesh is 1.1. The surface cell size on the side surfaces of the splitter plate ranges between 0.03 and 0.08. There are 20 layers of hexahedral elements within the plate.

A convergence study of the mesh resolution is carried out based on the meshes in Table 2. There are five meshes, Meshes 1-5, with different grid resolutions. These meshes are globally coarsen or refined with a refinement factor (RF) in reference to the baseline mesh – Mesh 3 outlined in Table 1. Moreover, it is of interest to understand whether the time step is small enough to provide converged results. Three values of the time step are set for Mesh 3. Another factor that might impact the simulation accuracy is the modelling of the geometric nonlinearity for the structure [23]. To clarify this impact, the nonlinear model is switched on or off for Mesh 3 with the different time step values, namely, Cases a–f for Mesh 3 in Table 2. The maximum Courant–Friedrichs–Lewy (CFL) numbers of all cases are less than one. Considering the largest time step of  $\Delta t/T = 5.13\text{e-}2$  for Mesh 5, the maximum CFL number is 0.36. As the cell sizes of Mesh 5 are smaller than the other meshes, its maximum CFL number is the largest amongst the cases.

The convergence is evaluated in terms of the maximum displacement of the splitter plate tip in the direction normal to the freestream flow direction,  $y_{tip,max}$ , and the frequency of the energy peak in the power spectral density (PSD) of the splitter-plate tip displacement,  $f_{res}$ . Fast Fourier transformation (FFT) is used for the PSD calculation. The total length of the signals is  $160T$ , where  $T$  is the time of the flow passing over the square cylinder. Each signal is divided into 15 segments with a overlapping rate of 50%. The sampling frequency is  $1000\text{Hz}$ . The Hanning window is used as the window function.

By comparing the cases of Meshes 1, 2, 3-a, 4 and 5 with the same settings such as the large deflection and  $\Delta t/T = 5.13\text{e-}2$  in Table 2, the maximum plate tip displacement  $y_{tip,max}$  and the peak frequency  $f_{res}$  are well converged with respect to the mesh resolution. In reference to Mesh 3-a of  $y_{tip,max}/D = 1.043$ , the deviations from the fine meshes Meshes 4 and 5 are 0.0085 and 0.0037. A similar convergence is also observed for  $f_{res}$ , which is 3.327 Hz in Mesh 3-a. Meshes 4 and 5 deviate from Mesh 3-a by  $-0.028$  and  $-0.071$  Hz.

Define the time-averaged absolute value of the splitter-plate tip displacement as

$$\bar{\psi} = \frac{1}{t_1 - t_0} \int_{t_0}^{t_1} |y_{tip}| dt, \quad (7)$$

where  $t_0$  is the time when the flow is fully developed, and  $(t_1 - t_0) = 226T$ . In reference to the results from the finest mesh resolution (Mesh 5), the error of  $\bar{\psi}$  from Mesh  $i$  (for  $i = 1, 2, 3\text{-a}, 4$ ) is defined as:

$$\% e_{\bar{\psi}}|_{\text{Mesh } i} = \frac{(\bar{\psi}|_{\text{Mesh } i} - \bar{\psi}|_{\text{Mesh } 5})}{\bar{\psi}|_{\text{Mesh } 5}} \times 100\% \quad (8)$$

By replacing  $\bar{\psi}$  with  $f_{res}$  in Eq. 8, the error of  $f_{res}$  from Mesh  $i$  is defined in a similar manner.

Based on Eq. 8, the errors of  $\bar{\psi}$  and  $f_{res}$  from the different mesh resolutions are plotted in Fig. 3, where Mesh 3 corresponds to Mesh 3-a in Table 2. As can be seen,



**Table 2** Results from different grid resolutions and numerical setups compared with the previous studies.

Mesh no.	$RF$	$N_{tot}$	LD	$\Delta t/T$	$y_{tip,max}/D$	$f_{res}$ [Hz]
Mesh 1	0.6	4274	yes	5.130e-2	1.0773	3.3630
Mesh 2	0.8	6740	yes	5.130e-2	1.0529	3.3390
Mesh 3-a	–	9408	yes	5.130e-2	1.0430	3.3270
Mesh 3-b	–	9408	no	5.130e-2	1.0867	3.2723
Mesh 3-c	–	9408	yes	2.565e-2	1.0264	3.2971
Mesh 3-d	–	9408	no	2.565e-2	1.1028	3.2175
Mesh 3-e	–	9408	yes	1.026e-2	1.0254	3.2798
Mesh 3-f	–	9408	no	1.026e-2	1.1349	3.1867
Mesh 4	1.2	12520	yes	5.130e-2	1.0345	3.2990
Mesh 5	1.4	19738	yes	5.130e-2	1.0393	3.2560
Wall [3]					1.12 ~ 1.32	2.78 ~ 3.26
Matthies and Steindorf [4]					1.0 ~ 1.35	3.13
Dettmer and Perić [5]					1.1 ~ 1.4	2.96 ~ 3.31
Olivier et al. [6]					0.95	3.165
Wood et al. [7]					1.1 ~ 1.2	2.78 ~ 3.13
Habchi et al. [9]					1.02	3.253

§ Here,  $RF$  is the refinement factor,  $N_{tot}$  the total number of cells,  $y_{tip,max}$  the maximum displacement of the splitter plate tip, and  $f_{res}$  the frequency of the plate structure response. The large deflection (LD) is switched on or off. The blue frame highlights the final choice used for the following analysis, that is, the baseline mesh in Table 1.

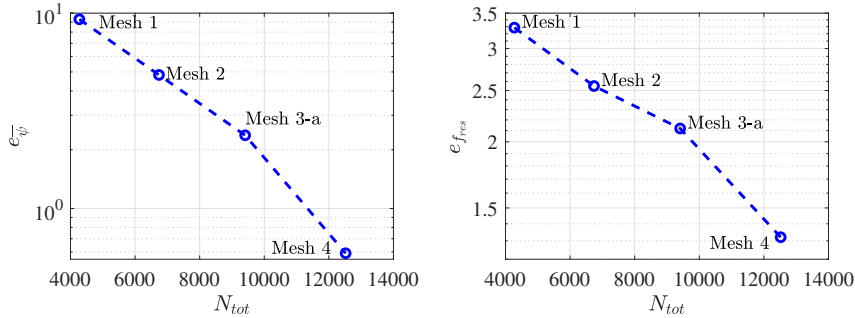


**Fig. 3** The errors of the time-averaged absolute tip displacement  $\bar{\psi}$  and the peak frequency of the tip displacement  $f_{res}$  from the different mesh resolution in reference to the finest mesh, Mesh 5, as a function of the total number of cells  $N_{tot}$ .

the errors decay exponentially with respect to the total number of cells  $N_{tot}$ . The trends suggest that the independence of the mesh resolution is achieved.

The influences of the geometric nonlinear structural modelling [23] are identified through the comparison of the cases on the basis of Mesh 3. The modelling is considered in Cases 3-a, 3-c and 3-e with the different time step sizes, but excluded from the other cases. According to the results in Table 2, disregarding the modelling leads to differences in  $y_{tip,max}$  and  $f_{res}$ , which are not negligible. Therefore, the nonlinearity associated with large deformations of the splitter plate is important for numerical accuracy. The modelling is involved in the simulations in the following analysis of the VIV.

**Table 3** Natural frequencies of the flexible splitter plate (unit: [Hz]).

Natural frequency	Analytical model	FEM
$f_{n,1}$	3.0288	3.2360
$f_{n,2}$	18.981	20.256
$f_{n,3}$	53.148	56.628

The time step size is adjusted in Cases 3-a – f of Mesh 3 to find out a feasible value. The results of Cases 3-a, 3-c and 3-e, where the geometric nonlinear structure model is accounted, show limited differences between them. Case 3-a with  $\Delta t/T = 5.13e-2$  provides  $y_{tip,max}/D = 1.043$ , whereas Cases 3-c and 3-e with smaller time step sizes provide 1.0264 and 1.0254. Moreover,  $f_{res}$  of Case 3-a is 3.327 Hz, which is similar to the other cases of 3.2971 and 3.2798. Besides that, although the geometric nonlinear model is excluded from Cases 3-b, 3-d and 3-f, the results of these cases with different time step sizes are similar. It is therefore reasonable to choose the time step size of  $\Delta t/T = 5.13e-2$  to guarantee both numerical accuracy and relatively shorter simulation time.

The cases of this study are also compared to the same scenario (i.e., the same configuration at  $Re=333$ ) simulated in previous studies [3–7, 9], as listed in Table 2. The present cases give  $y_{tip,max}/D = 1.0254 \sim 1.1349$ , and  $f_{res} = 3.1867 \sim 3.363$  Hz. These values are consistent with the previous results.

## 5 Results and Discussion

### 5.1 Modal analysis

A model analysis is performed for the flexible splitter plate using FEM and an analytical modelling method, i.e., the Euler-Bernoulli beam model [36]. It is assumed that there are no external forces, structural or viscous damping effects. In the analytical model, the general form of the  $n$ th mode shape reads:

$$\phi(x) = A\sin(\beta_n x) + B\cos(\beta_n x) + C\sinh(\beta_n x) + D\cosh(\beta_n x), \quad (9)$$

$$\beta_n^4 = \omega_n^2 m / (EI), \quad (10)$$

where  $m$  is the mass per unit length of the splitter plate,  $I$  the area moment of inertia of the plate section, and  $\omega_n$  the natural circular frequency. Given the upstream tip of the plate is imposed with zero displacement and rotation,  $\beta_n$  at the downstream tip of the plate satisfies:

$$\cos(\beta_n L)\cosh(\beta_n L) + 1 = 0, \quad (11)$$

where  $L$  denotes the length of the plate. Equation 11 is solved analytically to determine  $\omega_n$ .

The first three natural frequencies of the splitter-plate structure ( $f_{n,1}$ ,  $f_{n,2}$  and  $f_{n,3}$ ) computed using the two methods are presented in Table 3. In the FEM simulation, Mesh 3 is adopted. The FEM results are consistent with those of the analytical model. Small differences for about 6% between the methods are observed.

## 5.2 Unsteady FSI characteristics

Lift and drag forces of the configuration including both of the square body and splitter plate are analyzed by means of the trajectory evolution of the force coefficients in time. The lift coefficient is defined as  $C_L = f_y / (0.5\rho_f U_0^2)$ , and the drag coefficient as  $C_D = f_x / (0.5\rho_f U_0^2)$ . The trajectory evolution of  $C_L$  versus  $C_D$  for a variety of active oscillation frequencies  $f_{exc}$  is shown in Fig. 4. Here  $f_{exc}$  ranges between 0 and 6 Hz. The time-averaged drag coefficient  $C_{D,mean}$  and the root-mean-square (RMS) value of the lift coefficient  $C_{L,RMS}$  are marked out in this figure.

As shown in Fig. 4, the polar of  $C_L$  and  $C_D$  evolves in a closed simple trajectory as the square body is stationary, i.e.,  $f_{exc} = 0$  Hz. However, as  $f_{exc}$  is slightly increased to 0.25 Hz, the trajectory becomes disordered. It is enveloped within a region that has a similar overall shape but larger compared to that of the stationary case. This suggests larger lift and drag variations are introduced by the enforced body oscillation. The disordered status is sustained until  $f_{exc}$  increases up to 2.75 Hz. And the area spanned by the trajectory is increased with  $f_{exc}$ . A special case is found at 2.25 Hz, where the trajectory is comparatively less complex than the neighbor frequencies.

Clear single trajectories are also observed at  $f_{exc} \in [2.875, 3.5]$  Hz in Fig. 4. This phenomenon indicates that a lock-in effect appears because of the interaction between the plate structure and flow. The variation range of the trajectory is decreased as the frequency increases. The trajectory is almost collapsed into a curve at 2.875 Hz, while it becomes separated to form a butterfly shape at higher frequencies. The shapes of the trajectories at these high frequencies are different from that of the stationary case.

For  $f_{exc}$  above 3.5 Hz, Fig. 4 shows that disordered trajectories are excited again. The trajectory variation range first increases with respect to  $f_{exc}$  up to 4.25 Hz and, then, decreases with the frequency. This behavior is different compared to the disordered cases at the lower frequencies before the lock-in regime onsets, as discussed above. Moreover, the variation range at 3.625 Hz after the lock-in regime is much smaller than that at 2.75 Hz before the lock-in regime, but is relatively comparable to 0.25 and 6 Hz. A relatively less complex trajectory is seen at 4.5 Hz outside the lock-in regime. A similar effect also exists at 2.25 Hz below the lock-in frequencies.

The evolution history of the trajectories of the splitter-plate tip displacement,  $y_{tip}$ , and the lift coefficient,  $C_L$ , is displayed in Fig. 5. As can be seen, the trajectory of the stationary-cylinder case at  $f_{exc} = 0$  Hz does not follow a single loop. This behavior is contrary to the lift-drag trajectory identified in Fig. 4. A reason is that vortices bring about velocity and force fluctuations at high frequencies, which will be discussed later in spectral analysis.

It is clear in Fig. 5 that the trajectory becomes regularized as a single closed loop in the lock-in regime of  $f_{exc} \in [2.875, 3.5]$  Hz. Moreover, at 2.875 Hz where the lock-in regime onsets, the tip displacement is zero meter (i.e., at the neutral position of the splitter plate) when the lift force coefficient is zero. In contrast to this effect, at the other higher frequencies of the lock-in regime, the zero tip displacement is associated with non-zero lift coefficients. There are two points in the trajectory curve where the tip displacement is zero. They are dependent on the sides from which the plate returns to the neutral position. Besides, the trajectories at 2.25 and 4.5 Hz are less disordered

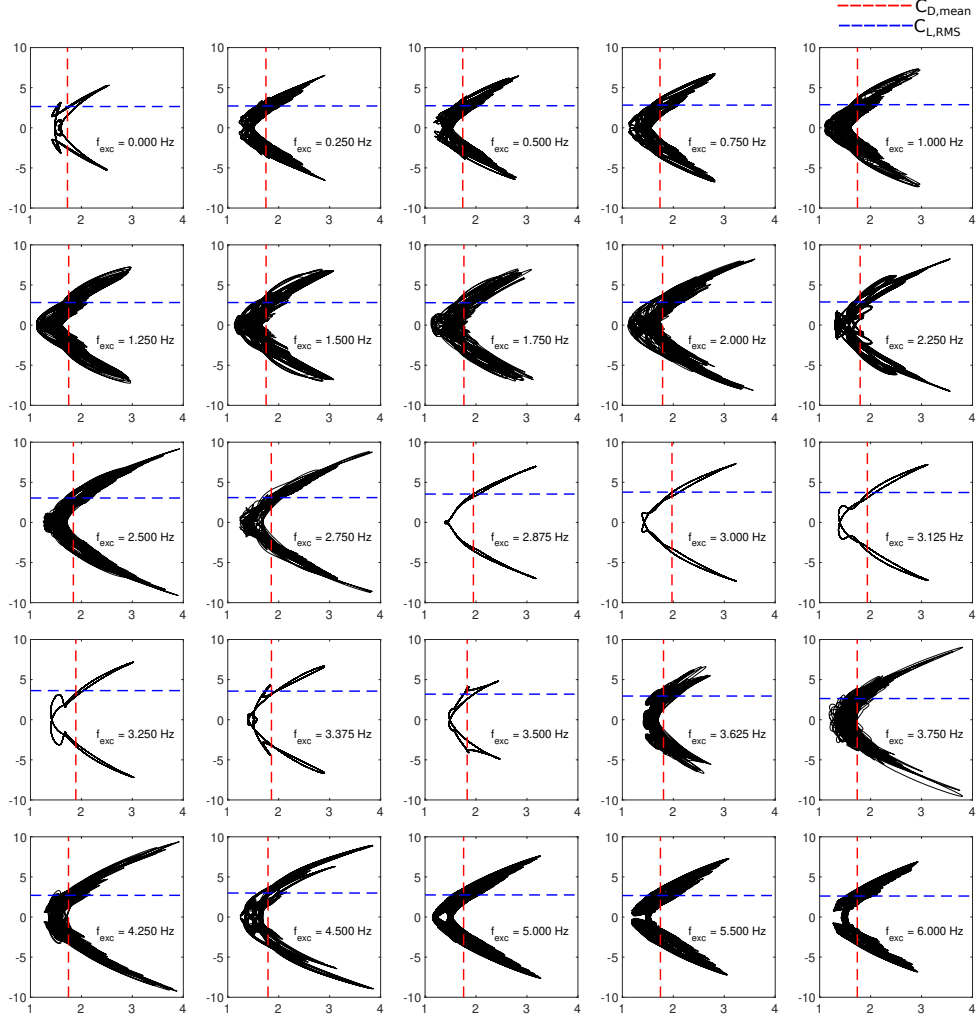


**Fig. 4** The trajectory evolution of  $C_L$  versus  $C_D$  in time. The x-axis is  $C_D$ , and the y-axis is  $C_L$ . The red and blue dash lines mark out  $C_{D,mean}$  and  $C_{L,RMS}$ .

than the neighbouring frequencies, although both frequencies are away from the lock-in regime. These behaviors agree with the findings for the lift-drag trajectories in Fig. 4.

Figure 6 displays the evolution history of the trajectory from the tip displacement and the drag coefficient  $C_D$ . The stationary case at  $f_{exc} = 0$  Hz also exhibits a simple trajectory. This is in line with the observation for the displacement versus  $C_L$  in Figs. 4 and 5, since flow vortices affect the drag and lift forces simultaneously.

A general observation in Fig. 6 is that the smallest  $C_D$  always appears at two positions of the plate tip that are located between the neutral and the maximum positions, but not at the neutral position. The reason is that vortices are subjected

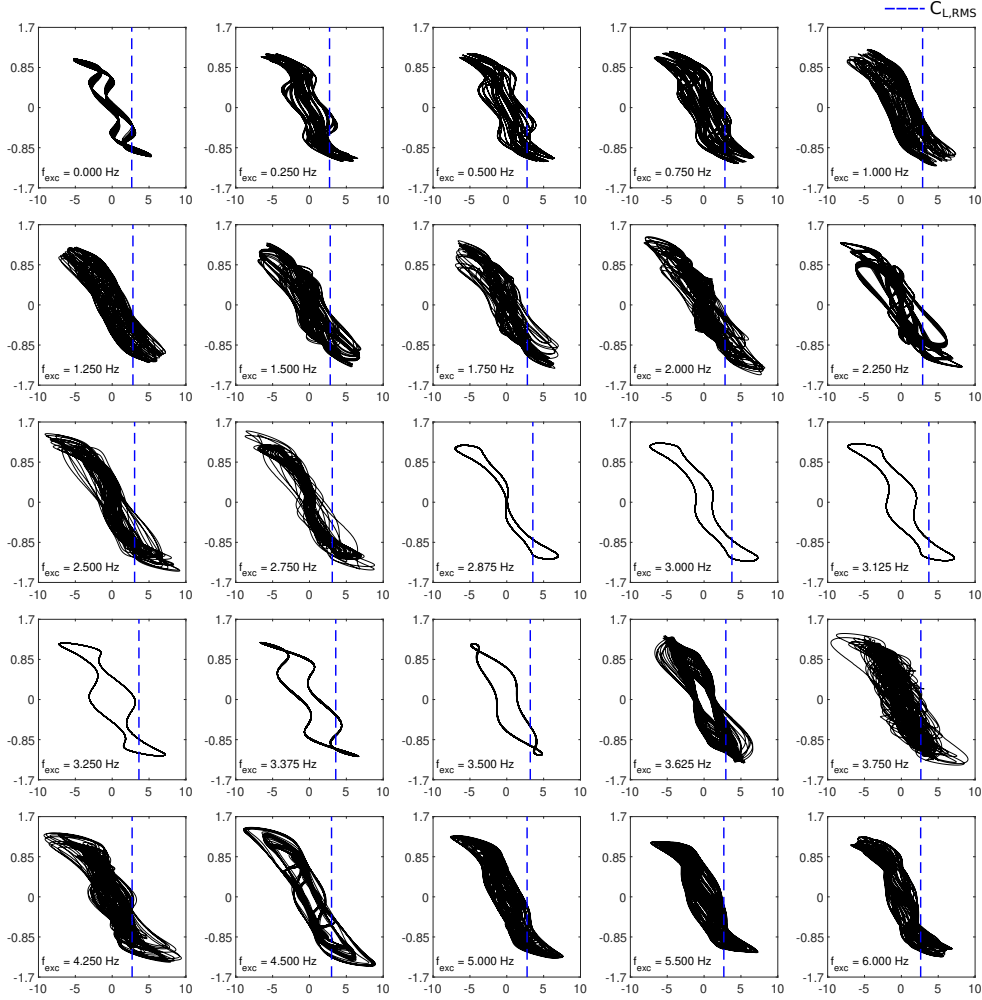


**Fig. 5** The trajectory evolution of  $y_{tip}/D$  versus  $C_L$  in time. The x-axis is  $C_L$ , and the y-axis is  $y_{tip}/D$ . The blue dash line indicates the RMS value of  $C_L$ .

to less constraints in the process to be swept downstream, when the splitter plate is pitched away from the neutral position. Furthermore,  $C_D$  increases rapidly as the plate tip approaches to the maximum deformation position, while it has the largest value before the plate tip reaches to the maximum position. This process indicates that the streamwise motion of vortices are confined by the pitch plate, resulting in the impingement of the vortices onto the plate. The impingement is increased quickly when the pitch process approaches the largest plate deformation.

As shown in Fig. 6, because of the lock-in, single close trajectories are seen at the enforced frequencies between 2.875 and 3.5 Hz. This effect is well consistent with the findings in Figs. 4 and 5. It is noticed in Fig. 6 that the area spanned by the trajectory

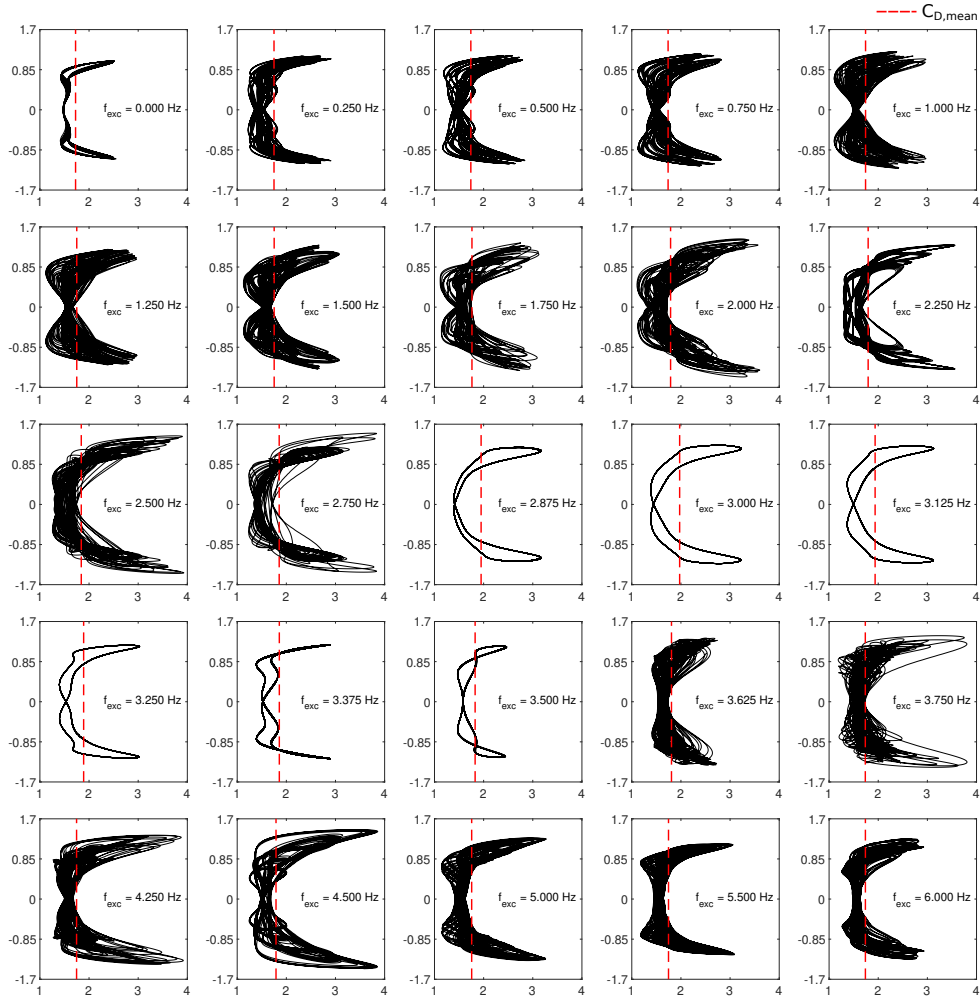


**Fig. 6** The trajectory evolution of  $y_{tip}/D$  versus  $C_D$  in time. The x-axis is  $C_D$ , and the y-axis is  $y_{tip}/D$ . The red dash line indicates the time-averaged value of  $C_D$ .

increases with the enforced frequency before the lock-in regime is reached. Then, in the lock-in regime, it grows with frequencies up to 3.125 Hz and, then, is narrowed down. After the regime, the area becomes larger again up to 4.5 Hz and decreases above this frequency. Additionally, the trajectories at 2.25 and 4.5 Hz are less disordered than the neighboring frequencies. These phenomena agree with the other evolutions in Figs. 4 and 5.

Snapshots of the z-component of the vorticity vector for several selected  $f_{exc}$  are illustrated in Fig. 7. These frequencies are 0, 2, 3.125, 4.25 and 6 Hz, which spread over the whole frequency range of interest including the lock-in regime. As can be seen, it is difficult to recognize obvious differences in the vortex development among these

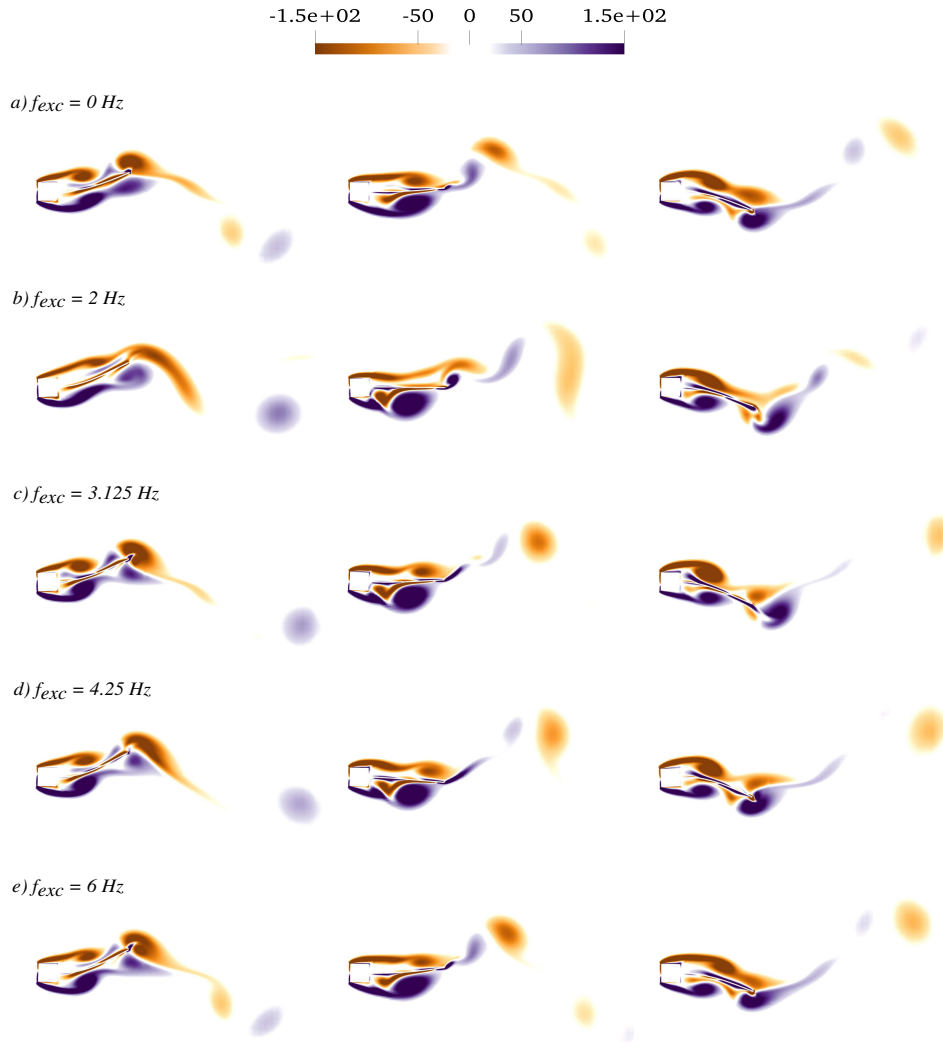


**Fig. 7** Snapshots of the vorticity component  $\omega_z$ . From left to right: approximately the position of the maximum tip displacement, the neutral position, and the position of the minimum tip displacement.

cases, even though according to the analysis above it has been addressed that the force coefficients and plate tip displacement behave in significantly distinct manners within and outside the lock-in regime. Hence, the quantitative data will be mainly discussed in the subsequent analysis.

The time series of the tip displacement  $y_{tip}$  and the velocity component  $u_y$ , which is normal to the freestream flow direction, at the probe point S2 are displayed in Fig. 8. The results of  $f_{exc} = 0, 2, 3.25$  and  $4.25$  Hz are chosen to show. Assuming the splitter

plate is rigid without any deformation, periodic sinusoidal displacement at the plate tip is obtained, and also shown in the figure to explore the potential coherence between the passive structure deformation and the active (enforced) structure oscillation (i.e., the pitch motion). The probe point is positioned in the wake downstream of the plate, and its coordinates are found in Fig. 2.

It is seen in Fig. 8 that the plate tip in the stationary case exhibits regular wavy displacements. The velocity component  $u_y$  in the wake in this case, however, fluctuates with an irregular wave shape, indicating that multiple frequencies exist in the fluctuations.

In the cases of the square cylinder enforced with  $f_{exc} = 2$  and 4.25 Hz outside the lock-in regime in Fig. 8,  $y_{tip}$  fluctuates with a variety of amplitudes and phases, which do not follow the enforced oscillation displacement (drawn with the red curves in the figure). The tip displacement in the case at 4.25 Hz shows more wave periods than that at 2 Hz. It suggests that the enforced pitch oscillation introduces fluctuations at more frequencies. Meanwhile, the fluctuations of  $u_y$  are much more irregular in both cases.

A specific case shown in Fig. 8 is the one at  $f_{exc} = 3.25$  Hz, which is located within the lock-in regime. As can be seen, the tip displacement fluctuates in a regular wave form. A constant phase shift is identified in the plate tip displacement in comparison to the enforced tip oscillation. The amplitude of the tip displacement is much larger than the enforced tip oscillation, since the large scale deformation of the flexible plate accounts for additional displacement at the plate tip. Moreover, the velocity component  $u_y$  at S2 in the wake exhibits periodic wave-like fluctuations. Small fluctuations are observed near the wave troughs and valleys. This implies the fluctuations at a relatively higher frequency because of vortices developed in conjunction with the upstream structure vibration.

### 5.3 Spectral analysis of FSI

The normalized PSDs of the velocity component  $u_y$  (denoted by  $\hat{S}_{u_y}$ ) at the probe points, S1, S2 and S3, for several cases are shown in Fig. 9, where the predominant peaks and corresponding frequencies are marked out. All PSDs in the different cases are normalized based on the maximum peak of S2 at 3.327 Hz in the stationary case ( $f_{exc} = 0$  Hz). The coordinates of the probe points are illustrated in Fig. 2. As noticed in Fig. 7, S1 is placed between two shear layers that are shed from the leading and trailing edges of the square body, respectively. The position of S3 is mainly inside the region over which the leading-edge vortices pass. S2 is contained in the wake downstream of the splitter plate.

In the stationary case in Fig. 9, two predominant peaks are observed at S1. The maximum peak at 6.653 Hz, and the smaller peak exists at 3.327 Hz, which is close to the first natural frequency of the splitter-plate structure of  $f_{n,1} = 3.236$  Hz. the smaller peak frequency is half of the other large peak frequency. The same maximum peak frequency at 6.653 Hz is also seen for S3. Despite a peak at 3.327 Hz also exists at S3, its normalized magnitude is nearly negligible than that at S1. Looking at S2, only one peak is recognized at 3.327 Hz. The results convey that the shear layer mainly contains vortices at the two frequencies identified in the PSDs. The vortices at the lower frequency are flushed down along the splitter plate and, then, excite the



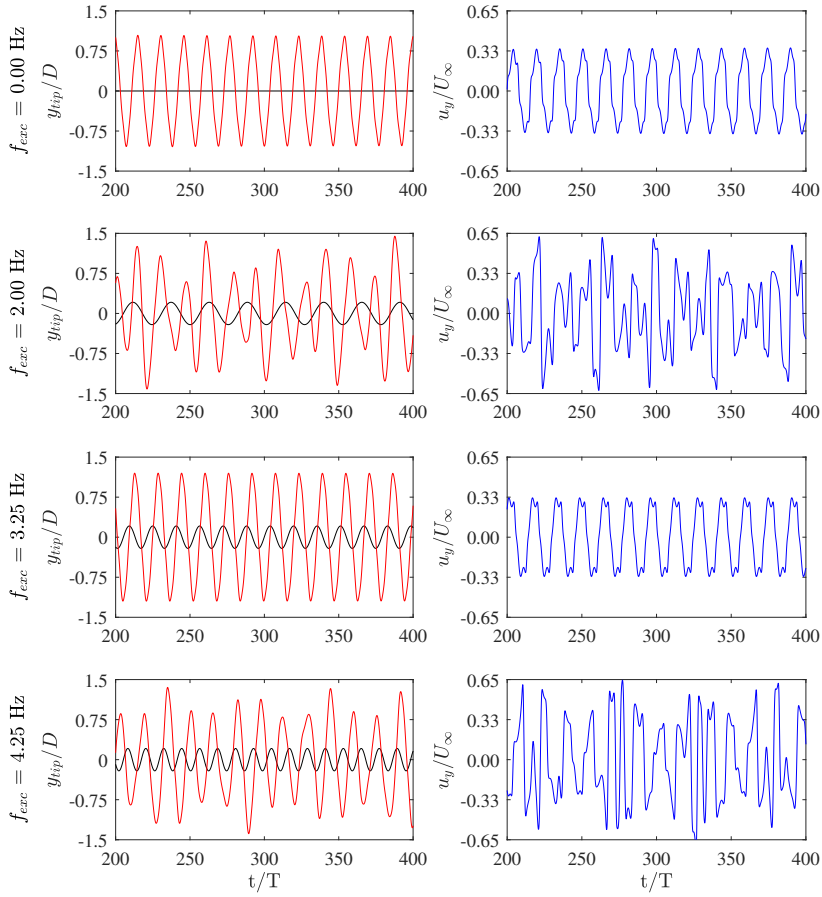


**Fig. 8** The time series of the normalized tip displacement  $y_{tip}/D$  and the normalized velocity component  $u_y/U_\infty$  at the probe point, S2, in the wake. The black curves in the left figures indicate the tip displacement of a rigid splitter plate.

plate vibration. Meanwhile, when the other vortices at the higher frequencies move downstream, they go outwards away from the splitter plate and therefore have a limited influence on the plate vibration. This effect is visualized in terms of the vorticity component  $\omega_z$  in Fig. 7. The probe point, S1, is in the region where the leading- and trailing-edge shear layers interact with each other, and the leading-edge vortices occur on the outer side with respect to those trailing-edge ones. Therefore, it is reasonable to deduce that S1 captures the characteristic frequencies of both shear layers, namely, the two predominant peak frequencies. And S3 presents the characteristic frequency of the leading-edge shear layer. At S2, the vortices from the two sides of the square

body merge together, and the merged wake is characterized with the peak frequency of 3.327 Hz.

In Fig. 9, the enforced case with  $f_{exc} = 2$  Hz show five significant peaks at S1. The multiple frequencies arise as the enforced frequency is outside the lock-in regime. Part of these frequencies such as 3.245 Hz is only identified at S2, and the others (5.245, 6.469 and 8.469 Hz) as well as 7.245 Hz at S3. This phenomenon suggests that S1 captures the flow characteristics at both S2 and S3. This effect is also found in the stationary case discussed above. By observing the enforced cases with  $f_{exc} = 3.25$  in the lock-in regime and 4.25 Hz above the regime, the same effect exists as well.

To understand the effects of the enforced pitch frequency on the characteristic frequencies of the tip displacement and the lift and drag forces, the PSDs of these variables are shown in Fig. 10. The results of each variable are normalized based on the largest peak magnitude of the respective PSD in the stationary case. As can be seen in the stationary case, the PSD of the lift force  $\hat{S}_L$  shows another smaller peak at 16.653 Hz, in addition to the peak at 3.327 Hz that is also observed for the velocity field in Fig. 9. The drag force  $\hat{S}_D$  has three peaks. The additional small high frequency peaks explain the reason why the trajectories in Figs. 4–6 are not completely single loops. Similar phenomenons are observed for the enforced cases, so the trajectories related to the lift and drag become disordered. Amongst all variables, the PSDs of the drag force exhibit more peaks than the tip displacement and lift force. This might be caused by the splitter plate interfering the shear layers detached from the leading edges of the square cylinder (see Fig. 7). A common effect in all cases is that the frequency of the major peak is near the natural frequency of the plate. However, for the enforced frequencies of  $f_{exc}$  at 2.75 and 3.75 Hz which are closed to the lock-in regime, the tip displacement is noticed with another peak with a large magnitude that exists near  $f_{exc}$ , and the lift force also presents a relatively large peak at the same frequencies. It means that the flow and structure interact at two characteristic frequencies. Thus, the trajectory of the tip displacement and lift force becomes disordered as found in Fig. 5. A special case is at  $f_{exc} = 3.625$  Hz which is the upper bound of the lock-in regime. Only one significant peak exists for both tip displacement and lift force, but several very small peak commence. This leads to a disordered trajectory as well. When  $f_{exc} = 0.25$  and 5 Hz, which are far from the lock-in regime, secondary peaks at the enforced frequencies become small.

In Fig. 11, the RMS lift coefficient  $C_{L,RMS}$ , the time-averaged drag coefficient  $C_{D,mean}$  and the RMS drag coefficient  $C_{D,RMS}$  are plotted as a function of  $f_{exc}$ . All the three coefficients change in similar trends: the magnitudes gradually increase and reach to the largest value at  $f_{exc} = 3$  Hz. Above this frequency, the magnitudes drop fast to become similar to that in the stationary case. Recalling the lock-in regime for  $f_{exc} \in [2.875, 3.5]$  Hz indicated in Fig. 4, it is therefore found that the fast increase and drop of the large magnitudes are triggered due to the lock-in effect. The large RMS values of the lift and drag coefficients imply that flow vortices and structure deformations are intensively interacted at specific frequencies. Therefore, remarkable energy from the flow is absorbed by the splitter-plate structure. It is worth noting that the frequency of the largest coefficients is 3 Hz rather than the one like 3.25 Hz that is closer to the first natural frequency of the splitter plate  $f_{n,1} = 3.236$  Hz. The reason

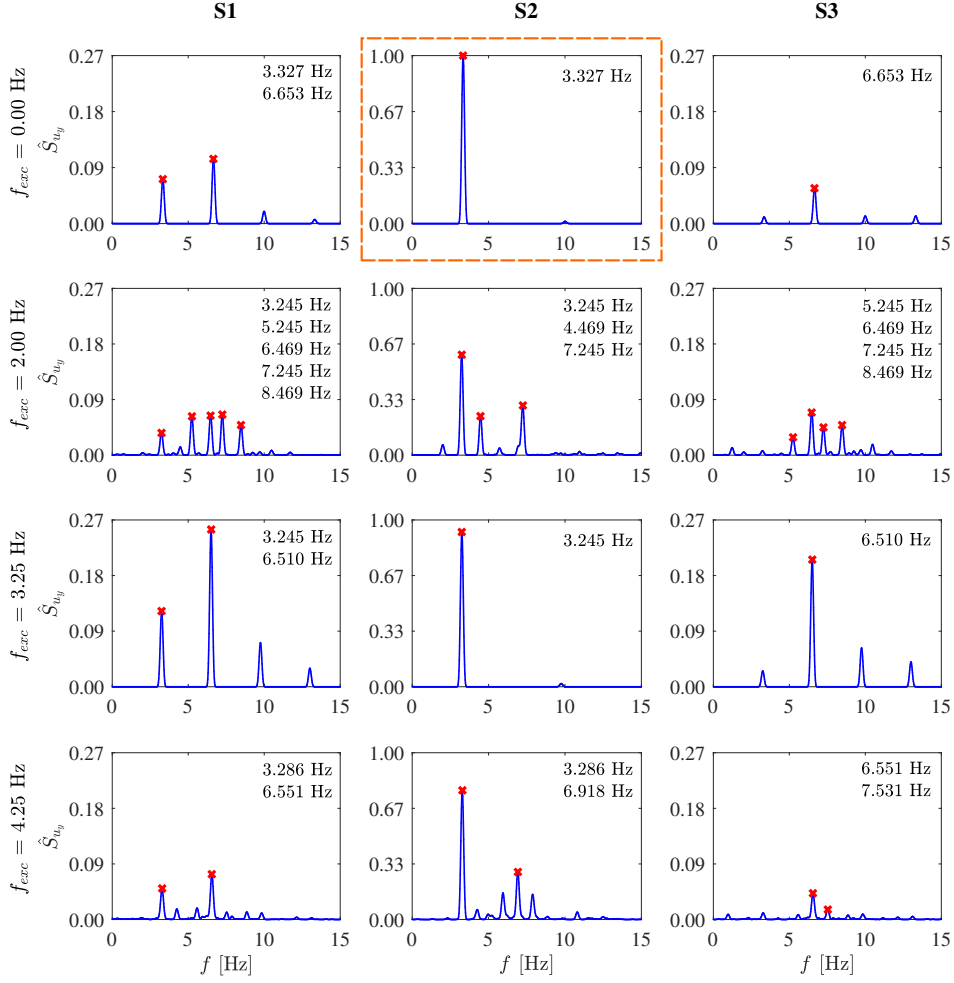


**Fig. 9** The normalized PSDs of the velocity component  $u_y$  at the probe points S1, S2 and S3 (from left to right) at various  $f_{exc}$ . The PSDs are normalized by the peak magnitude at 3.327 Hz of the PSD at S2 in the stationary case, which is encircled by the dashed box in orange. The predominant peaks are marked out with red cross symbols, and the corresponding frequencies are listed aside.

is associated with the combined effects of the passive VIV and active pitch oscillation, which will be explained in the following discussion. Moreover, another obvious increase starting from 4.25 Hz outside the lock-in regime is observed, and leads to a local maximal magnitude at 4.5 Hz. Above this frequency, the coefficients decrease even though the enforced oscillation is enhanced by increasing  $f_{exc}$ .

Figure 12 shows the dominant peak frequencies obtained from the normalized PSDs of the lift force,  $\hat{S}_L$ , in the enforced oscillation frequency range between 0 and 6 Hz, and the symbols plotted are colored based on the normalized peak magnitudes. The

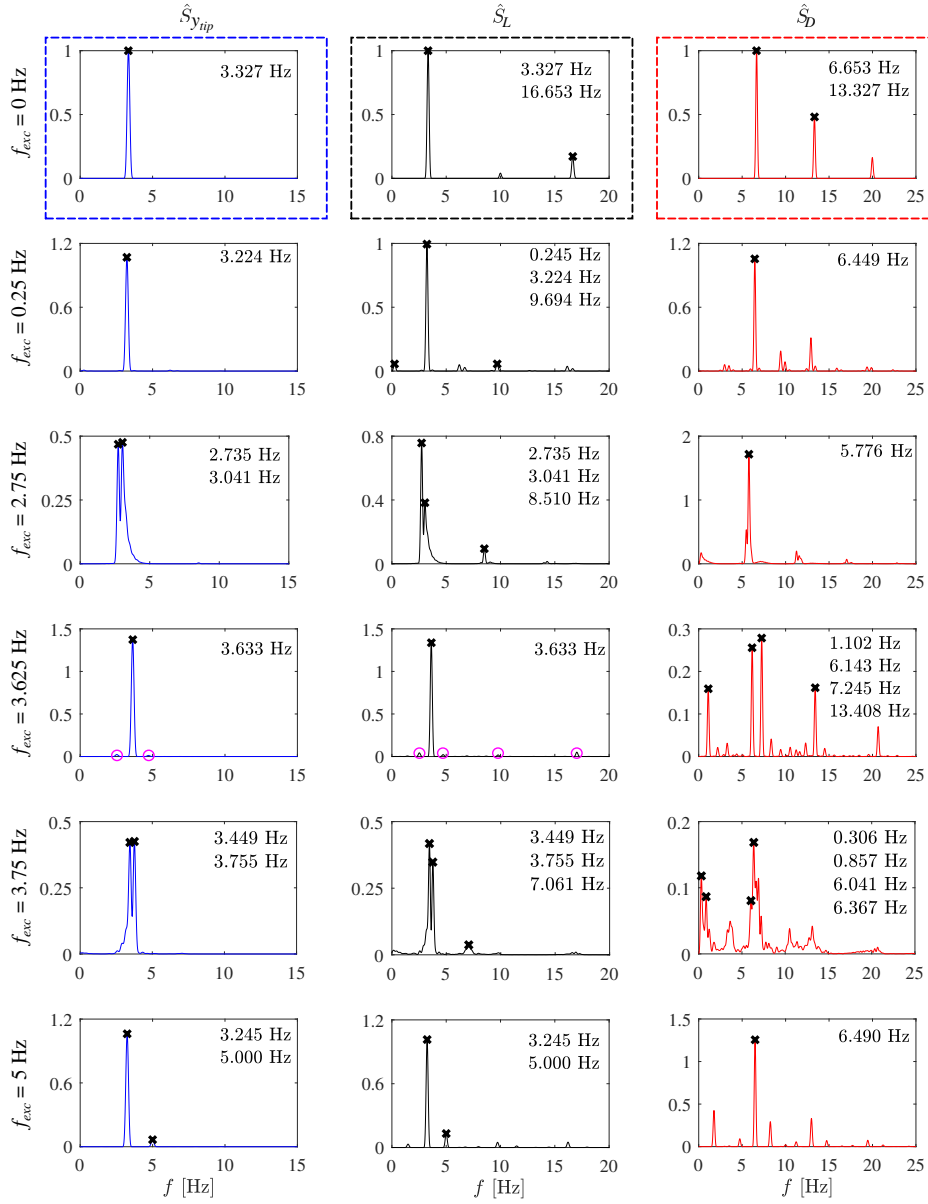


**Fig. 10** The normalized PSDs of the tip displacement ( $\hat{S}_{y_{tip}}$ ), the lift force ( $\hat{S}_L$ ) and the drag force ( $\hat{S}_D$ ) at different  $f_{exc}$ . The PSDs of each variable are normalized in reference to those at  $f_{exc} = 0$  Hz, which are displayed within the dashed boxes. The cyan circles in the plots at  $f_{exc} = 3.625$  Hz mark the peaks that have nearly negligible amplitudes.

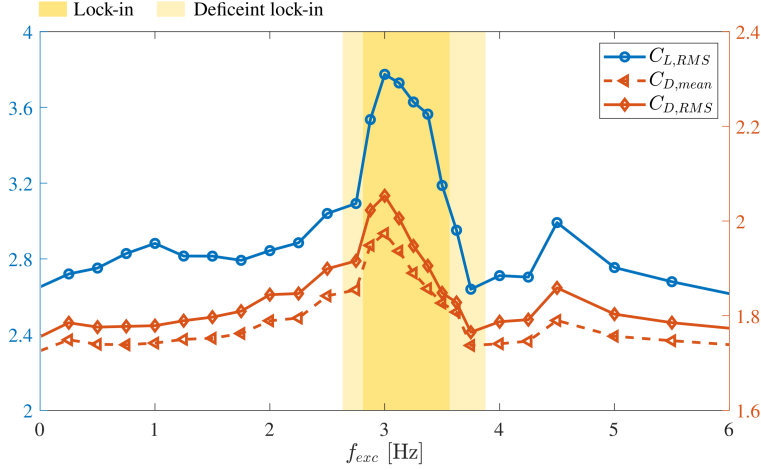


**Fig. 11** The RMS lift coefficient,  $C_{L,RMS}$ , and the time-averaged and RMS drag coefficients,  $C_{D,mean}$  and  $C_{D,RMS}$ , as a function of the enforced oscillation frequency  $f_{exc}$ .

normalization is made on the basis of the PSD peak magnitude of the stationary case, where only one peak is observed at  $f_L = 3.327$  Hz (see Fig. 10). The first natural frequency of the splitter plate,  $f_{n,1} = 3.236$  Hz from the FEM presented in Table 3, is chosen as a reference to evaluate the resultant characteristic frequencies. Here  $f_{L,M}$  denotes the frequency of the largest peak, and  $f_{L,L}$  and  $f_{L,R}$  are the frequencies of the secondary peaks below and above  $f_{L,M}$ , respectively. The criterion to choose the peaks is that peak magnitudes should be larger than 5% of the largest peak magnitude in a PSD spectrum. In other words, small peaks below the critical value are disregarded. In the lock-in regime,  $f_{L,M}$  is equal to the enforced oscillation frequency  $f_{exc}$ . This suggests that the force generation is only controlled by the active pitch oscillation. Furthermore, the peak magnitudes in the lock-in regime are larger than those outside the regime. Especially, the largest magnitude is noticed at  $f_{exc} = 3$  Hz, where the largest values of  $C_{L,RMS}$ ,  $C_{D,RMS}$  and  $C_{D,mean}$  are also found (see Fig. 11).

However, for  $f_{exc} = 2.75$ ,  $3.625$  and  $3.75$  Hz that are outside but to next to the lock-in regime, the frequencies of the predominant structural response are still equal to  $f_{exc}$ . There are two different effects at these frequencies in comparison with the lock-in. First, a secondary peak frequency  $f_{L,R}$  is seen for  $f_{exc} = 2.75$  Hz, while  $f_{L,L}$  for  $3.75$  Hz. The other effect is that the peak magnitudes are much smaller than those in the lock-in regime. Secondary frequencies are invisible for  $f_{exc} = 3.625$  Hz, since the peaks (which are marked out with cyan circles for  $\hat{S}_L$  in Fig. 10) are too small to consider based on the evaluation criterion given above. These secondary peak frequencies lead to the disordered trajectories, as observed in Figs. 4 and 5. Given these special effects, it is deemed that semi-lock-in regimes are formed around these enforced frequencies.

As illustrated in Fig. 12, another interesting phenomenon is that for  $f_{exc}$  outside of the lock-in and semi-lock-in regimes (that is, in the non-lock-in regimes),  $f_{L,M}$  is

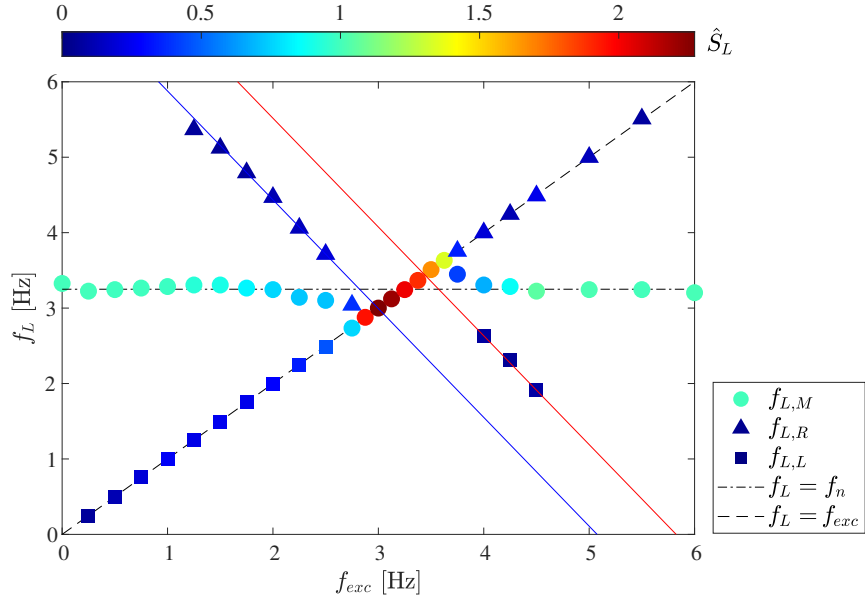


**Fig. 12** The maximum peak frequency in the PSDs of the lift force,  $f_{L,M}$ , and the secondary peak frequencies,  $f_{L,L}$  and  $f_{L,R}$ , with respect to  $f_{exc}$ . The symbols are colored with the normalized magnitudes of the PSDs,  $\hat{S}_L$ , at these frequencies. The dash-dotted line marks out the natural frequency of the plate of  $f_{n,1} = 3.236$  Hz; the blue and red solid lines are drawn based on the ratio of  $\Delta f_L / \Delta f_{exc} = -1$ .

always identified around the first natural frequency of the splitter plate  $f_{n,1}$ . Moreover, secondary peak frequencies of both  $f_{L,L}$  and  $f_{L,R}$  are clearly visible. Even more interestingly, the secondary peak frequencies are distributed along the line defined by  $f_L = f_{exc}$ , as well as the two lines (colored in blue and red in the figure) following the ratio of  $\Delta f_L / \Delta f_{exc} = -1$ . Note that another ratio of  $\Delta f_L / \Delta f_{exc} = 1$  is derived from  $f_L = f_{exc}$ . Thus, the flow field is influenced by the combined effects of the passive structural characteristics and the active pitch oscillation. The largest peak magnitude of  $\hat{S}_L$  amongst all of the cases is observed at  $f_{exc} = 3$  Hz, but not at another enforced frequency that is more close to  $f_{n,1}$ . By looking at the lines highlighted in the figure, this enforced frequency is located at the intersection point of the lines following  $f_L = f_{exc}$  and the  $-1$  ratio.

#### 5.4 Structural responses of the splitter plate

The values of  $f_{res}$  for the most predominant peaks in the normalized PSDs,  $\hat{S}_{ytip}$ , are plotted with respect to  $f_{exc}$  in Fig. 13. The normalization is based on the magnitude of the dominant peak in the stationary case with  $f_{exc} = 0$  Hz. Here  $f_{res,M}$  denotes the frequency of the largest peak, and  $f_{res,L}$  and  $f_{res,R}$  are the frequencies of the second or third largest peaks below and above  $f_{res,M}$ , respectively. The criterion to choose

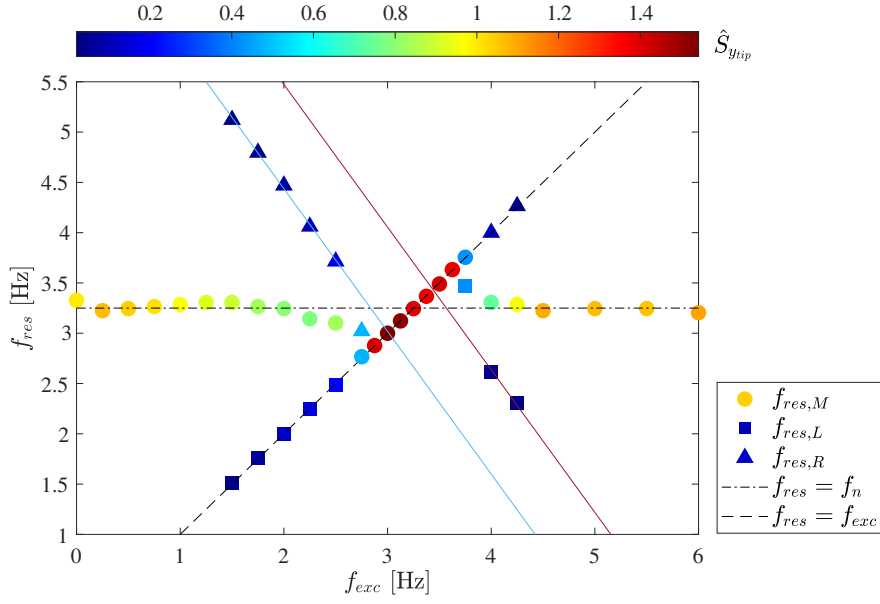


**Fig. 13** The peak frequencies (i.e., the maximum peak frequency  $f_{res,M}$ , the secondary peak frequencies  $f_{res,L}$  and  $f_{res,R}$  below and above  $f_{res,M}$ ) of the normalized plate-tip displacement PSD  $\hat{S}_{ytip}$  with respect to  $f_{exc}$ . The symbols are colored with the normalized magnitudes of the PSDs,  $\hat{S}_{ytip}$ , at these frequencies. The dash-dotted line indicates the natural frequency of the plate of  $f_{n,1} = 3.236$  Hz; the blue and red solid lines are plotted based on the ratio of  $\Delta f_{res}/\Delta f_{exc} = -1$ .

the peaks is that peak magnitudes should be larger than 2% of the largest magnitude in the respective PSD spectrum. The symbols in the figure are colored with the PSD magnitudes. The first natural frequency,  $f_{n,1} = 3.236$  Hz computed using the FEM (see Table 3), is defined as a reference point for the evaluation. The FFT for computing the spectra of the splitter-plate tip displacements adopts the same signal processing parameters and setup as those used to do the spectral analysis for  $f_{res}$  in Table 2.

As shown in Fig. 13, in the range of  $f_{exc}$  from 2.75 to 3.75 Hz, the values of  $f_{res}$  are aligned with the relationship of  $f_{res,M} = f_{exc}$ , namely, the ratio of  $\Delta f_{res,M}/\Delta f_{exc} = 1$ . This trend is also observed for the lift force PSDs in Fig. 12. The frequency range covers the lock-in and semi-lock-in regimes according to the analysis of the lift force PSDs. This suggests that the enforced pitch oscillation plays an important role in controlling the energy absorption of the structure. The oscillation dominates the resonant responses of the splitter-plate structure, which significantly interact with flow vortices. This specific lock-in effect due to the enforced pitch is different from classical lock-in effects found in the VIV of the benchmark stationary case at  $f_{exc} = 0$  Hz [37, 38] or a stationary circular cylinder [23, 37]. In these stationary blunt body scenarios where

the freestream velocity  $U_0$  can be adapted within a wide range at low Reynolds numbers, the frequencies of the lock-in regime are found being dependent on the reduced velocity ratio  $U_0/(f_{n,1}D)$ .

Like the frequency distribution of  $\hat{S}_L$  (see Fig 12), an interesting phenomenon for the non-lock-in regimes in Fig. 13 is that apart from the most dominant peak  $f_{res,M} \approx f_{n,1}$ , two secondary peaks  $f_{res,L}$  and  $f_{res,R}$  are identified in the non-lock-in frequencies of  $f_{exc}$  ranging from 1.5 to 2.5 Hz and from 4 to 4.25 Hz. These secondary peaks are distributed along three lines with the ratios of  $\Delta f_{res}/\Delta f_{exc} = \pm 1$ , where the ratio of 1 is derived from  $f_{res} = f_{exc}$ . Moreover, secondary peaks are not identified at comparatively lower and higher enforced frequencies of  $f_{exc} \leq 1.25$  Hz and  $\geq 4.5$  Hz. Therefore, the passive structural responses determined by the natural frequencies are mainly significant in the non-lock-in regimes, in particular at frequencies far from the lock-in regime. In contrast, in the lock-in and semi-lock-in regimes, the effects of the enforced pitch oscillation overwhelm the passive responses and furthermore, determine the energy conversion from the flow to the structure deformation.

## 6 Discussions

To confirm the ratios of  $\Delta f_{res}/\Delta f_{exc} = \pm 1$ , Fig. 14 shows the absolute differences between the secondary peak frequencies ( $f_{res,L}$  and  $f_{res,R}$ ) and the predominant peak  $f_{res,M}$  as a function of the enforced oscillation frequency  $f_{ext}$ . The left peak difference is calculated as  $\Delta f_{res,L} = f_{res,M} - f_{res,L}$ , and the right peak difference as  $\Delta f_{res,R} = -f_{res,M} + f_{res,R}$ . According to the analysis for Fig. 13, the secondary peak frequencies appear at  $f_{exc}$  from 1.5 to 2.5 Hz and from 4 to 4.25 Hz. Examples for the calculation at  $f_{exc} = 2.25$  and 4 Hz are illustrated in Fig. 14. As can be seen in this figure,  $\Delta f_{res,L}$  and  $\Delta f_{res,R}$  are nearly equal to each other at every enforced frequency of interest. In other words, the two secondary peak frequencies,  $f_{res,L}$  and  $f_{res,R}$ , are nearly symmetric with respect to the frequency of the largest peak  $f_{res,M}$ , resulting in the ratios of  $\pm 1$ . The same effects have also been observed for the lift force PSDs  $\hat{S}_L$ , while the data are not plotted here for the sake of brevity.

Comparing all the cases in terms of the magnitudes of the most predominant peaks in the lift force PSDs (see Fig. 12) and the tip displacement PSDs (see Fig. 13), the smallest values are found at  $f_{exc} = 2.75$  and 3.75 Hz outside the lock-in regime. The cases with these two enforced frequencies as well as 3.625 Hz exhibit that  $f_{L,M}$  and  $f_{res,M}$  are dependent on  $f_{exc}$  like those in the lock-in regime. On the other hand, as indicated in Figs. 4–6, the trajectories of the tip displacement, lift and drag become disordered at these enforced frequencies. This is because a secondary peak commences to play a role, which is identified in Fig 10. Additionally, as found in Fig 11, the force coefficients of  $C_{L,RMS}$ ,  $C_{D,mean}$  and  $C_{D,RMS}$  alter obviously at these enforced frequencies. By synthetically considering all of these effects,  $f_{exc} = 2.75$ , 3.625 and 3.75 Hz are therefore deemed to be in semi-lock-in regimes, which exist next to the lock-in regime.

Considering the lines following the ratios of  $\pm 1$  in Fig. 12 or 13, two intersection points of the lines are located at  $f_{exc} = 3$  and 3.44 Hz. These frequencies are very closed to the frequency limits of the lock-in regime, which are 2.875 and 3.5 Hz. Thus, it is deduced that the onset of the lock-in effects is associated with the conditions at



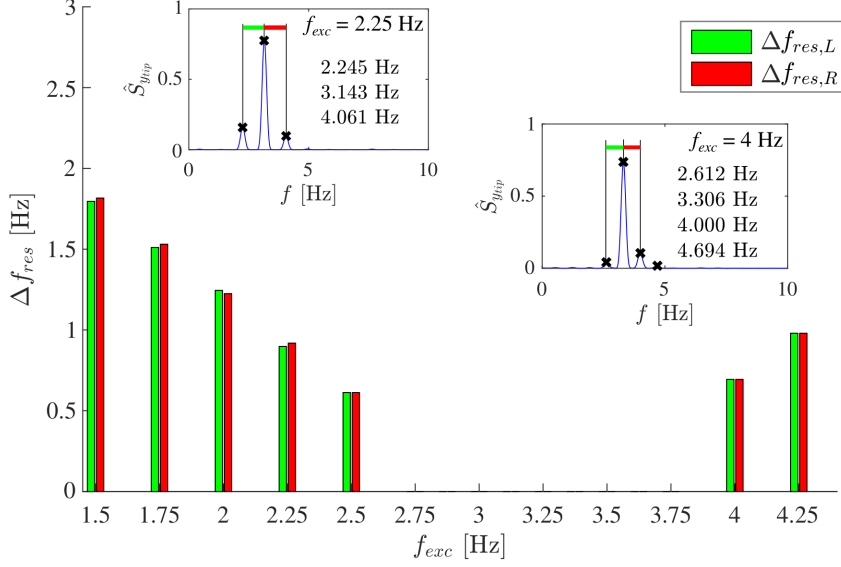


**Fig. 14** The absolute differences between the secondary peak frequencies of the splitter-plate structural responses ( $f_{res,L}$  and  $f_{res,R}$ ) and the largest peak frequency  $f_{res,M}$ , as a function of the enforced oscillation frequency  $f_{exc}$ . These frequencies are referred to Fig. 13.

the intersection points. At  $f_{exc} = 3$  Hz, the largest peak magnitude presents in both  $\hat{S}_L$  and  $\hat{S}_{y_{tip}}$ . And the peak magnitudes in the semi-lock-in regimes in both PSDs are smaller than those in the lock-in and non-lock-in regimes.

For the lift force and tip displacement, the common relationships explored to determine the peak frequency distribution in the PSDs are summarized as follows. Here, either  $f_L$  or  $f_{res}$  is simply signified as  $f$  for brevity.

- If  $f_{exc}$  is in the lock-in regime,

$$f_M = f_{exc} \Rightarrow \Delta f_M / \Delta f_{exc} = 1. \quad (12)$$

- If  $f_{exc}$  is in the semi-lock-in regimes,

$$\begin{cases} f_M = f_{exc} \Rightarrow \Delta f_M / \Delta f_{exc} = 1 \\ f_R \in (f_M, f_{n,1}) \text{ \& invisible } f_L, & \text{for } f_{exc} < f_{cr,min} \\ f_L \in (f_{n,1}, f_M) \text{ \& invisible } f_R, & \text{for } f_{exc} > f_{cr,max} \end{cases} \quad (13)$$

Here  $f_{cr,min}$  and  $f_{cr,max}$  are the minimum and maximum critical values of the enforced frequency for the lock-in regime. In the current study,  $f_{cr,min}$  is around 2.875 Hz, and  $f_{cr,max}$  around 3.5 Hz. Note that for  $f_{exc} = 3.625$  Hz,  $f_L$  is also invisible because of the negligible spectral magnitude at this frequency (see Fig. 10).

- If  $f_{exc}$  is outside the lock-in regime,

$$\begin{cases} f_M \approx f_{n,1} \\ f_i = f_{exc} \Rightarrow \Delta f_i / \Delta f_{exc} = 1, & i = L \text{ or } R. \\ \Delta f_i / \Delta f_{exc} = -1 \end{cases} \quad (14)$$

## 7 Conclusions

The combination of the passive VIV and active pitch oscillation is investigated for a square cylinder assembled with a flexible splitter plate at a low Reynolds number of 333. The enforced oscillation frequency,  $f_{exc}$ , ranges from 0 to 6 Hz, and the oscillation amplitude is kept as a constant of  $3^\circ$ . The stationary-cylinder case for this configuration with  $f_{exc} = 0$  Hz has been widely investigated as a benchmark VIV case. This facilitates the validation of the method used in this study and, furthermore, the understanding on how the actively enforced pitch oscillation affects the VIV in reference to the stationary-cylinder case.

The trajectories of the lift and drag coefficients evolving in time are disordered, except for the stationary case and those with  $f_{exc}$  between 2.875 and 3.5 Hz where the trajectories are in simple closed loops. Even though a very low frequency of 0.25 Hz is enforced, the lift and drag are affected. The area within which a disordered trajectory varies is dependent on  $f_{exc}$ . Likewise, the trajectories of the splitter-plate tip displacement with respect to either lift or drag exhibit similar behaviors. Based on the trajectory patterns, a lock-in regime of  $f_{exc} \in [2.875, 3.75]$  Hz is deduced, since the simple closed loops indicate the lock-in interaction between the flow and the splitter plate. The zero lift and the smallest drag in the lock-in regime are achieved on most occasions when the tip of the splitter plate is at non-neutral position, while an exception is at 2.875 Hz where the lift is not zero.

The RMS values of the lift coefficient and the RMS and time-averaged values of the drag coefficient show similar trends in the dependence on  $f_{exc}$ . A remarkable change of these values is found in the lock-in regime. The coefficients become the largest at 3 Hz, which implies the most significant lock-in interaction being excited, despite that the first natural frequency of the splitter plate is  $f_{n,1} = 3.236$  Hz.

For the cases with  $f_{exc} = 2.75, 3.625$  and 3.75 Hz, the flow and structural vibrations show special features mixing lock-in and non-lock-in effects. As in the lock-in regime, the frequencies of the largest peaks in the PSDs of the lift force and tip displacement are nearly equal to the corresponding  $f_{exc}$ . However, the magnitudes of the largest peaks are smaller than in all other cases. Since a secondary peak frequency onsets, the trajectories of the tip displacement with respect to the lift and drag forces become disordered, as in the non-lock-in regime. The time-averaged and RMS values of the force coefficients also alter significantly. Therefore, the regimes encompassing these enforced frequencies are deemed as semi-lock-in regimes.

By extracting the predominant peak frequencies  $f_L$  from the PSDs of the lift force, it is found that these frequencies are distributed by following three characteristic relationships such as  $f_L \approx f_{n,1}$ ,  $f_L = f_{exc}$  (i.e.,  $\Delta f_L / \Delta f_{exc} = 1$ ), and  $\Delta f_L / \Delta f_{exc} = -1$ . In the lock-in regime, only one predominant peak at  $f_{L,M}$  presents in every case,

and it satisfies  $f_{L,M} = f_{exc}$ . This relationship is also found in the semi-lock-in regimes, while additionally a secondary peak appears at a frequency between  $f_{L,M}$  and  $f_{n,1}$ . In the non-lock-in regimes,  $f_{L,M} \approx f_{n,1}$ ; and the frequencies of the two secondary predominant peaks,  $f_{L,L}$  and  $f_{L,R}$ , are distributed to follow  $f_L = f_{exc}$  and the ratio of  $\Delta f_L / \Delta f_{exc} = -1$ . Moreover, the characteristic lines intersect with each other at  $f_{exc} = 3$  and 3.44 Hz, which are very closed to the frequency limits of the lock-in regime. And the largest peak magnitude amongst all the cases presents at  $f_{exc} = 3$  Hz. These results suggest that the onset of the lock-in effects is triggered by the conditions at the intersection points.

The tip displacement exhibits the same spectral characteristics as those found for the lift force. The characteristic relationships addressed for the lift force and tip displacement infer that the interaction between the flow and current configuration is dependent on the combined effects of the passive VIV and actively enforced pitch oscillation. On the other hand, in the specific lock-in regime caused by adjusting  $f_{exc}$ , only the enforced pitch oscillation dominates the interaction.

Based on a simple canonical configuration, the present study explores special FSI characteristics as passive structure vibrations excited by flow are combined with active control of structure pitch motions. Nonetheless, the study has not analyzed the parameters such as the pitch magnitude, the center of rotation, the length of the splitter plate, Reynolds numbers, and so forth. Their effects are interesting to address in future work. Furthermore, when high Reynolds numbers are concerned, more complex simulations in three dimensions with the aid of turbulence modelling techniques will be requested to solve relevant issues.

## Acknowledgement

We thank Dr. Rameez Badhurshah and Dr. Massoud Tatar for discussions on VIV. This work received funding from Chalmers University of Technology Foundation for the strategic research project "Hydro- and Aerodynamics". The computations and data handling were enabled by resources provided by the Swedish National Infrastructure for Computing (SNIC), partially funded by the Swedish Research Council through grant agreement no. 2018-05973.

## Declaration of Interests

The authors report no conflict of interest.

## References

- [1] Yu, Y., Liu, Y., Amandolese, X.: A review on fluid-induced flag vibrations. *Applied Mechanics Reviews* **71**, 010801–1 (2019)
- [2] Nilsson, S., Yao, H.-D., Karlsson, A., Arvidson, S.: Effects of viscosity and density on the aeroelasticity of the ONERA M6 wing from subsonic to supersonic speeds. *AIAA Aviation 2022 Forum*, 27 June – 1 July, Chicago, USA, 2022–3670 (2022)

- [3] Wall, W.A.: Fluid-struktur-interaktion mit stabilisierten finiten elementen. PhD thesis, University of Stuttgart (1999)
- [4] Matthies, H.G., Steindorf, J.: Partitioned strong coupling algorithms for fluid-structure interaction. *Computers & structures* **81**(8-11), 805–812 (2003)
- [5] Dettmer, W., Perić, D.: A computational framework for fluid-structure interaction: finite element formulation and applications. *Computer methods in applied mechanics and engineering* **195**(41-43), 5754–5779 (2006)
- [6] Olivier, M., Morissette, J.-F., Dumas, G.: A fluid-structure interaction solver for nano-air-vehicle flapping wings. In: 19th AIAA Computational Fluid Dynamics, pp. 2009–3676 (2009)
- [7] Wood, C., Gil, A., Hassan, O., Bonet, J.: Partitioned block-Gauss-Seidel coupling for dynamic fluid-structure interaction. *Computers & structures* **88**(23–24), 1367–1382 (2010)
- [8] Kassiotis, C., Ibrahimbegovic, A., Niekamp, R., Matthies, H.G.: Nonlinear fluid–structure interaction problem. Part I: implicit partitioned algorithm, nonlinear stability proof and validation examples. *Computational Mechanics* **47**, 305–323 (2011)
- [9] Habchi, C., Russeil, S., Bougeard, D., Harion, J.-L., Lemenand, T., Ghanem, A., Della Valle, D., Peerhossaini, H.: Partitioned solver for strongly coupled fluid-structure interaction. *Computers & Fluids* **71**, 306–319 (2013)
- [10] Schott, B., Ager, C., Wall, W.A.: A monolithic approach to fluid-structure interaction based on a hybrid Eulerian-ALE fluid domain decomposition involving cut elements. *arXiv cs.CE*, 1808-003431 (2018)
- [11] Yao, H.-D., Svensson, M.Y., Nilsson, H.: Deformation of dorsal root ganglion due to pressure transients of venous blood and cerebrospinal fluid in the cervical vertebral canal. *Journal of Biomechanics* **76**, 16–26 (2018)
- [12] Binyet, E.M., Chang, J.-Y., Huang, C.-Y.: Flexible plate in the wake of a square cylinder for piezoelectric energy harvesting – parametric study using fluid-structure interaction modeling. *Energies* **13**, 2645 (2020)
- [13] Binyet, E., Huang, C.-Y., Chang, J.-Y.: Water tunnel study of a cantilever flexible plate in the wake of a square cylinder. *Microsystem Technologies* **26**, 3435–3449 (2020)
- [14] Furquan, M., Mittal, S.: Flow past two square cylinders with flexible splitter plates. *Computational Mechanics* **55**, 1155–1166 (2015)
- [15] Sarioglu, M.: Control of flow around a square cylinder at incidence by using a

- splitter plate. *Flow Measurement and Instrumentation* **53**, 221–229 (2017)
- [16] Turki, S.: Numerical simulation of passive control on vortex shedding behind square cylinder using splitter plate. *Engineering Applications of Computational Fluid Mechanics* **2**(4), 514–524 (2008)
- [17] Ali, M.S.M., Doolan, C.J., Wheatley, V.: Low reynolds number flow over a square cylinder with a splitter plate. *Physics of Fluids* **23**, 033602 (2011)
- [18] Turek, S., Hron, J.: Proposal for numerical benchmarking of fluid-structure interaction between an elastic object and laminar incompressible flow. In: Bungartz, H., Schäfer, M. (eds.) *Fluid-Structure Interaction. Lecture Notes in Computational Science and Engineering* vol. 53. Springer, ??? (2006). [https://doi.org/10.1007/3-540-34596-5\\_15](https://doi.org/10.1007/3-540-34596-5_15)
- [19] Giannelis, N.F., Vio, G.A.: Computational benchmark of commercial fluid-structure interaction software for aeroelastic applications. In: *International Forum on Aeroelasticity and Structural Dynamics (IFASD) 2015, June 28 – July 02, 2015, Saint Petersburg, Russia*, pp. 2015–91 (2015)
- [20] Sahu, T.R., Furquan, M., Mittal, S.: Numerical study of flow-induced vibration of a circular cylinder with attached flexible splitter plate at low Re. *Journal of Fluid Mechanics* **880**, 551–593 (2019)
- [21] Pfister, J.-L., Marquet, O.: Fluid-structure stability analyses and nonlinear dynamics of flexible splitter plates interacting with a circular cylinder flow. *Journal of Fluid Mechanics* **896**, 24 (2020)
- [22] Duan, F., Wang, J.: Fluid–structure–sound interaction in noise reduction of a circular cylinder with flexible splitter plate. *Journal of Fluid Mechanics* **920**, 6 (2021)
- [23] Mittal, C., Sharma, A.: Flow-induced vibration of a flexible splitter-plate in the wake of a stationary cylinder. *Physics of Fluids* **33**(11), 113607 (2021)
- [24] Frei, S., Holm, B., Richter, T., Wick, T., Yang, H.E.: *Fluid-structure Interaction : Modeling, Adaptive Discretisations and Solvers*, 1st edn. Walter de Gruyter GmbH, Berlin/Boston (2017)
- [25] W., H.C., A., A.A., J., C.: An arbitrary Lagrangian-Eulerian computing method for all flow speeds. *Journal of Computational Physics* **14**, 227–253 (1974)
- [26] Farhat, C., Geuzaine, P., Grandmont, C.: The discrete geometric conservation law and the nonlinear stability of ALE schemes for the solution of flow problems on moving grids. *Journal of Computational Physics* **174**(2), 669–694 (2001)
- [27] Fernández, M.A., Gerbeau, J.-F., Grandmont, C.: A projection semi-implicit

- scheme for the coupling of an elastic structure with an incompressible fluid. *International Journal for Numerical Methods in Engineering* **69**, 794–821 (2007)
- [28] Quaini, A., Quarteroni, A.: A semi-implicit approach for fluid-structure interaction based on an algebraic fractional step method. *Mathematical Models and Methods in Applied Sciences* **17**(6), 957–983 (2007)
- [29] de Boer, A., van Zuijlen, A.H., Bijl, H.: Comparison of conservative and consistent approaches for the coupling of non-matching meshes. *Computer Methods in Applied Mechanics and Engineering* **197**(49), 4284–4297 (2008) <https://doi.org/10.1016/j.cma.2008.05.001>
- [30] Patankar, S.V., Spalding, D.B.: A calculation procedure for heat, mass and momentum transfer in three-dimensional parabolic flows. *International Journal of Heat and Mass Transfer* **15**(10), 1787–1806 (1972)
- [31] Zienkiewicz, O.C., Taylor, R.L., Zhu, J.Z.: *The Finite Element Method: Its Basis and Fundamentals*, 7th edn. Elsevier Butterworth-Heinemann, Oxford (2013). <https://doi.org/10.1016/C2009-0-24909-9>
- [32] Finlayson, B.A.: *The Method of Weighted Residuals and Variational Principles*, 1st edn. Academic Press, New York (1972)
- [33] Stroud, A.H., Secrest, D.: *Gaussian Quadrature Formulas*. Prentice-Hall, Englewood Cliffs, N.J. (1966)
- [34] Ramm, E., Wall, W.: Fluid-structure interaction based upon a stabilized (ALE) finite element method. In: *4th World Congress on Computational Mechanics: New Trends and Applications*, CIMNE, Barcelona, pp. 1–20 (1998)
- [35] Bazilevs, Y., Calo, V.M., Hughes, T.J., Zhang, Y.: Isogeometric fluid-structure interaction: theory, algorithms, and computations. *Computational mechanics* **43**(1), 3–37 (2008)
- [36] Rao, S.S.: *Vibration of Continuous Systems*. John Wiley & Sons, ??? (2019)
- [37] Kundu, A., Soti, A.K., Garg, H., Bhardwaj, R., Thompson, M.C.: Computational modeling and analysis of flow-induced vibration of an elastic splitter plate using a sharp-interface immersed boundary method. *SN Applied Sciences* **2**, 1110 (2020)
- [38] Kumar, D., Sen, S.: Flow-induced vibrations of a pair of in-line square cylinders. *Physics of Fluids* **33**, 043602 (2021)